High Diffusivity Lithium Intermetallic in Two-Phase Alloy Negative Electrode for Solid-State Batteries

Jack Aspinall[1], Fuhui Shen[2], Matthew Burton[1], Pranay Shrestha[1], Hua Guo[1], Souhardh Kotakadi[1], Yang Tu[2], Emily Milan[1], Pierre-Olivier Autran[3], Johannes Ihli[1], Yuichi Aihara[4], Laurence Brassart[2], Emilio Martínez Pañeda[2], and Mauro Pasta[1,*]

[1]Department of Materials, University of Oxford, Parks Road, Oxford OX1 3PH, United Kingdom
[2]Department of Engineering Science, University of Oxford, Parks Road, Oxford OX1 3PH, United Kingdom
[3]European Synchrotron Radiation Facility, 71 Avenue des Martyrs, Grenoble, France
[4]Nissan Research Centre, Nissan Motor Co., Ltd., Natsushima, Yokosuka, Kanagawa 237-8523, Japan

[*]Corresponding author: mauro.pasta@materials.ox.ac.uk

Supplementary information

Supplementary note 1: Intermetallic Selection

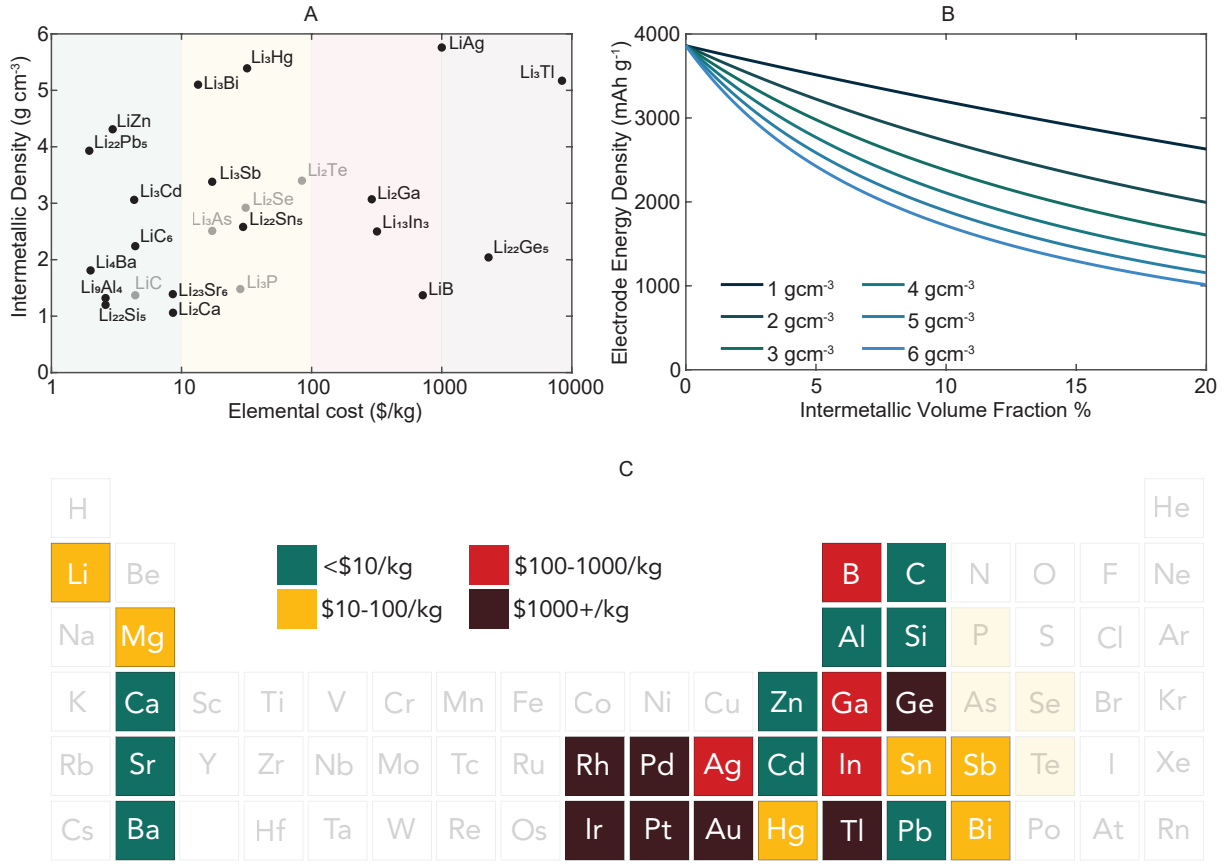

Figure S1: (a) Ragone plot of alloy element cost and density of intermetallic in equilibrium with lithium metal. (b) Impact on energy density for varied intermetallic density and volume fraction, when incoporated within lithium metal electrode, assumes no accessible capacity in intermetallic. (c) Reduced periodic table showing lithium alloy elements colored by element cost.

It is worth considering alternative elements which may form lithium-rich intermetallics with the requisite transport properties. Figure S1A shows a reduced periodic table of elements which alloy with lithium to form intermetallics or solid solutions in colour, and the remaining elements greyed out. Magnesium and silver form solid solutions with lithium up to 69 atomic % and somewhere near 9 atomic % respectively [1, 2]), the remaining alloying elements form intermetallics. Arsenic, phosphorus, selenium and tellurium form lithium compounds such as Li_3As, Li_2C_2, Li_3P, Li_2Se and Li_2Te, these are semiconductors, with significant band gaps but may have some electronic conductivity if precipitates are nanoscale [3]. The remaining elements have been colored according to their elemental cost. Many are prohibitively expensive, such as boron (B), gallium (Ga) and indium (In) [4]. Figure S1B plots the elemental cost against the density of the intermetallic in equilibrium with lithium metal on a Ragone plot. Of most interest for batteries are low density, low cost intermetallics. Bismuth is relatively cheap but is the heaviest non-radioactive metal, Li_3Bi has comparatively high density of 5.1 gcm^{-3}. Of lighter and cheaper intermetallics, antimony (Sb), cadmium (Cd) and lead (Pb) are highly toxic. A 1977 study showed antimony Li_3Sb compound has high diffusion kinetics at 360 °, but a very narrow solid solubility window of 0.04% [5]. Whilst toxicity isn't prohibitive as both lead and cadmium have a history of use in batteries, the most interesting alloying elements are aluminium (Al), calcium

(Ca), silicon (Si), strontium (Sr), tin (Sn) and zinc (Zn). Recent literature suggests that the Li_9Al_4, $Li_{21}Si_5$ and $Li_{23}SR_6$ compounds have slow diffusion kinetics compared to lithium, only forming electrochemically at elevated temperatures [6–8]. It may be possible to use the metastable LiAl phase, or equivalents, in combination with lithium metal. A separate study has estimated the diffusion coefficient of Li in Li_2Ca as 2.5×10^{-12} [9] by fitting electrochemical impedance spectra on self-symmetric Li_2Ca cells.

A 1987 study measured the chemical diffusion coefficient for LiZn and $Li_{22}Sn_5$ at ambient temperature. [10] LiZn is reported to have a diffusion coefficient from 3.7×10^{-9} to 5.0×10^{-10} cm^2s^{-1}. $Li_{4.4}Sn$ has a solid solubility in the range $Li_{4.35–4.48}Sn$, twice as wide as that of Li_3Bi, and a chemical diffusion coefficient from 1.8×10^{-7} to 5.9×10^{-7} cm^2s^{-1}. Of the explored binary intermetallics, Li_3Bi and $Li_{22}Sn_5$ are the most promising, $Li_{22}Sn_5$ has a lower chemical diffusivity compared to Li_3Bi but also a lower density and wider solubility window. Contemporary work on the lithium diffusion kinetics and solid solubility window of these intermetallics and others, including ternary intermetallics, is needed.

Supplementary note 2: Thermodynamic factor derivation

The thermodynamic factor is defined as:

$$\Gamma = (\partial \ln a_{Li})/(\partial \ln c_{Li}) \tag{S1}$$

The full cell reduction relative to a lithium metal counter is defined as:

$$Li_3Bi + \delta \cdot Li_{counter} \rightarrow Li_{(3+\delta)}Bi \tag{S2}$$

From the Nernst equation:

$$E = E^0 - \frac{RT}{F} \ln Q \tag{S3}$$

$$Q = \ln\left(\frac{a_{Li}^{Li_{3+\delta}Bi}}{a_{Li}^{Li} \cdot a_{Li}^{Li_3Bi}}\right) \tag{S4}$$

Activity of lithium in the standard molar states for lithium metal and Li_3Bi is equal to 1.

$$E(c) = E^0 - \frac{RT}{F} \cdot \ln(a_{Li}^{Li_{3+\delta}Bi}) \tag{S5}$$

Rearrange in terms of activity of lithium in the $Li_{3+\delta}Bi$ phase:

$$\ln(a_{Li}) = \frac{F}{RT}(E^0 - E(c)) \tag{S6}$$

Differentiate both sides with respect to $\ln(c_{Li})$.

$$\Gamma = \frac{\partial \ln(a_{Li})}{\partial \ln(c_{Li})} = -\frac{F}{RT} \cdot \frac{\partial E(c_{Li})}{\partial \ln(c_{Li})} \tag{S7}$$

We can separate the final term into its constituent derivatives

$$\frac{\partial E(c_{Li})}{\partial \ln(c_{Li})} = \frac{\partial E(c_{Li})}{\partial \delta} \cdot \frac{\partial \delta}{\partial \ln(c_{Li})} \tag{S8}$$

The molar concentration of lithium in $Li_{3+\delta}Bi$ is given by:

$$c_{Li} = \frac{3+\delta}{V_m} \tag{S9}$$

Therefore,

$$\ln(c_{Li}) = \ln\left(\frac{1}{V_m}\right) + \ln(3+\delta) \tag{S10}$$

$$\frac{\partial \ln(c_{Li})}{\partial \delta} = \frac{1}{3+\delta} \tag{S11}$$

Substituting this in gives the final expression.

$$\Gamma = \frac{\partial \ln(a_{Li})}{\partial \ln(c_{Li})} = -\frac{F(3+\delta)}{RT} \cdot \frac{\partial E}{\partial \delta} \tag{S12}$$

Supporting figures

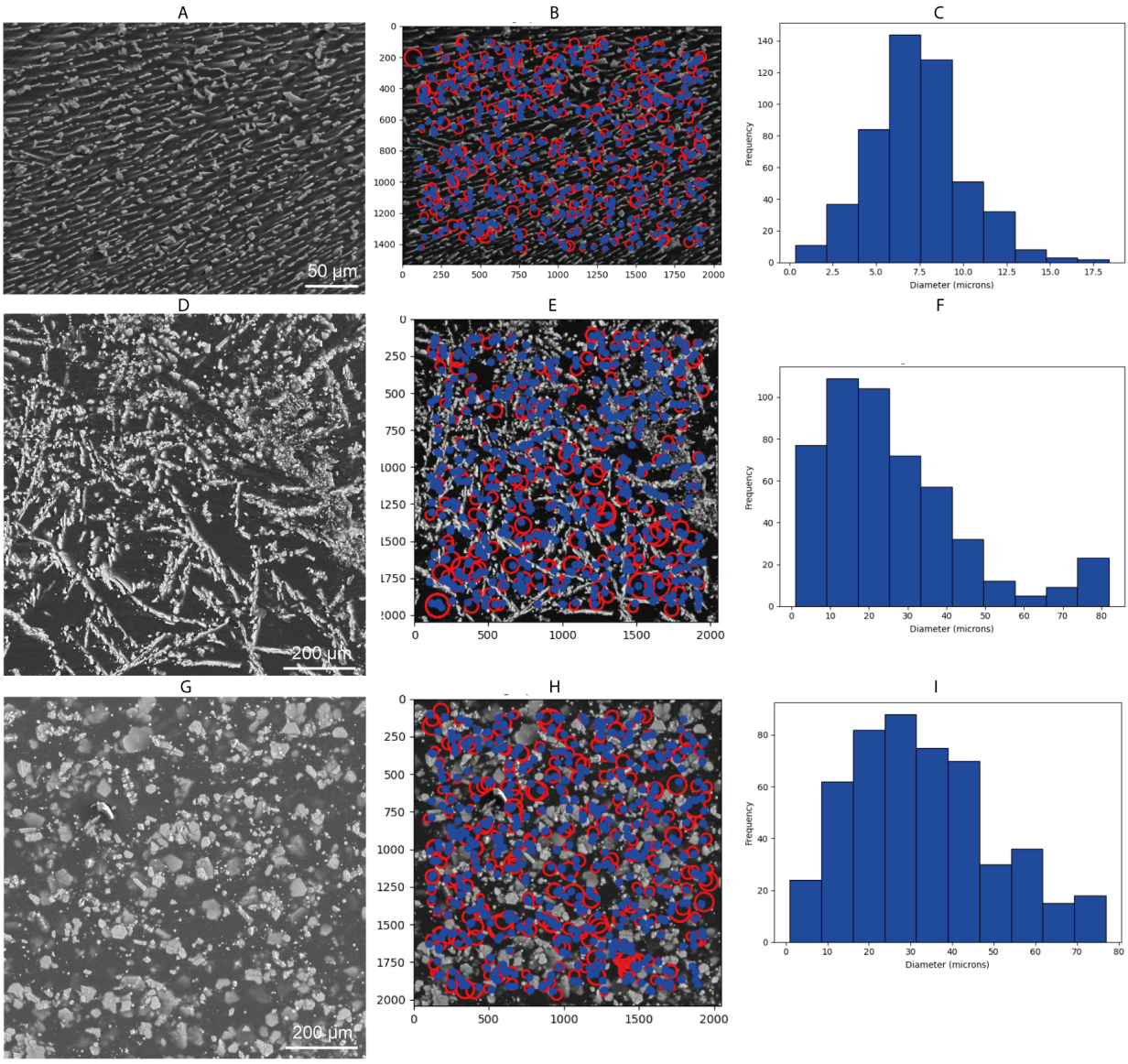

Figure S2: (a) Micrograph of as-cast Li+7.6%Zn alloy. (b) 500 fitted circles within lithium metal phase for as-cast Li+7.6%Zn alloy.. (c) Histogram of circle diameters for as-cast Li+7.6%Zn alloy. (d-f) Equivalent for as-cast Li+2.75%Bi alloy. (g-i) Equivalent for calendared Li+2.75%Bi alloy.

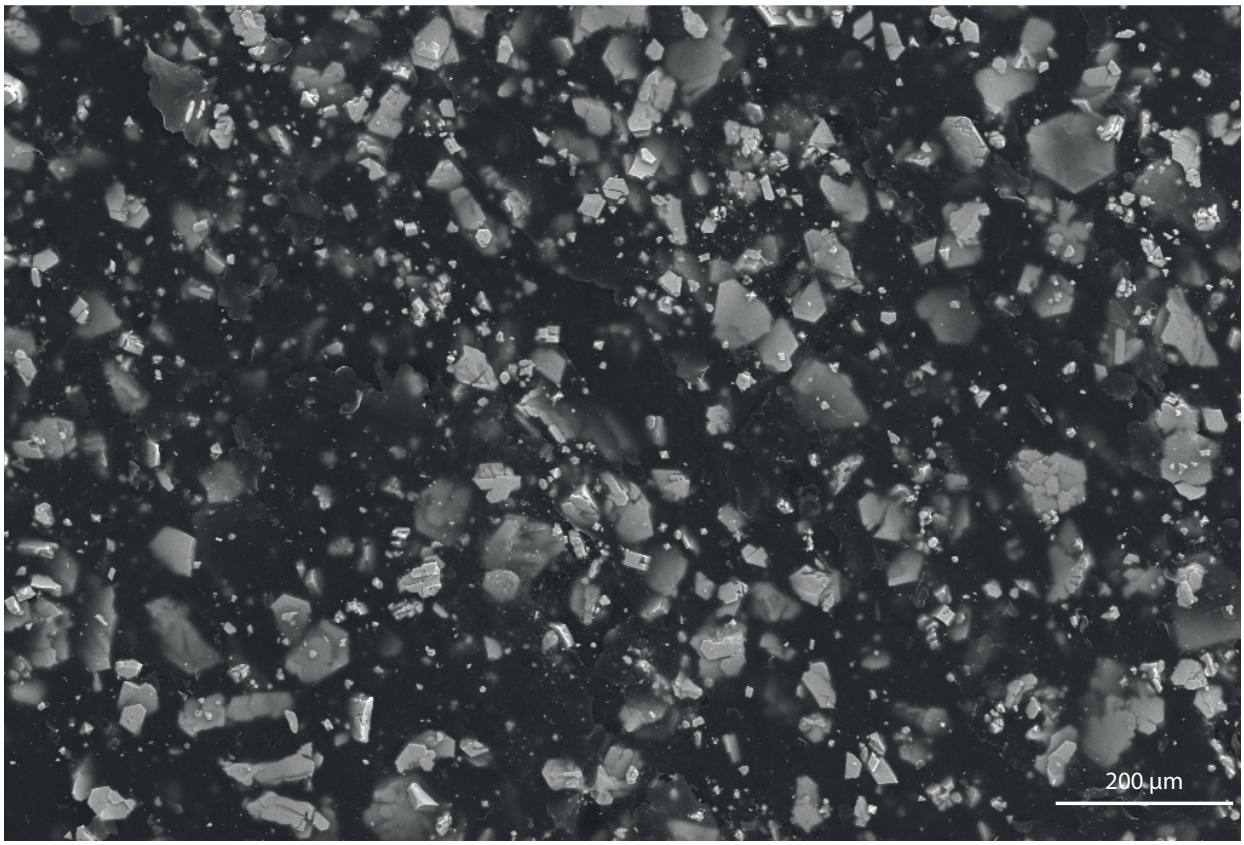

Figure S3: Scanning electron micrograph of oil quenched Li+1%Mg+2.75%Bi. 30 kV beam voltage, secondary electron.

Supplementary note 3: Hexagonal Li_3Bi Isomorph

It's interesting to consider whether the h-Li_3Bi phase is thermodynamically stable across any part of the temperature range. All samples produced at the Li_3Bi composition show only the cubic Li_3Bi phase, figure S5, and this remained true after annealing c-Li_3Bi ball milled powder at 900°C for 3 hours (some LiBi was observed from lithium loss on annealing). Chemically lithiated bismuth powder with 1M Li-biphenyl solution in tetrahydrofuran (THF) at ambient temperature also formed the cubic Li_3Bi phase. [11] These results suggest c-Li_3Bi is the thermodynamically stable bulk phase at ambient temperature and that heating to 900 °C and then cooling doesn't stabilise the hexagonal phase. In the similar Li-Sb system, hexagonal h-Li_3Sb is marginally more stable across all temperatures (7 meV at 298 K) than c-Li_3Sb, but slight pressure has been shown to stabilise the cubic phase. [12] When cooling Li+Bi alloys from the very high temperatures needed to achieve melt homogeneity, the h-Li_3Bi is somehow stabilised - this could be due to interfacial energy effects or tensile stresses. Approximating stoichiometric composition for both, h-Li_3Bi has a 9% lower density ($\rho_{h\text{–}Li_3Bi} = 4.60\ \mathrm{g\,cm^{-3}}$, $\rho_{c\text{–}Li_3Bi} = 5.01\ \mathrm{g\,cm^{-3}}$). Despite this, we could not distinguish regions of the two phases based on density contrast in either tomography or SEM.

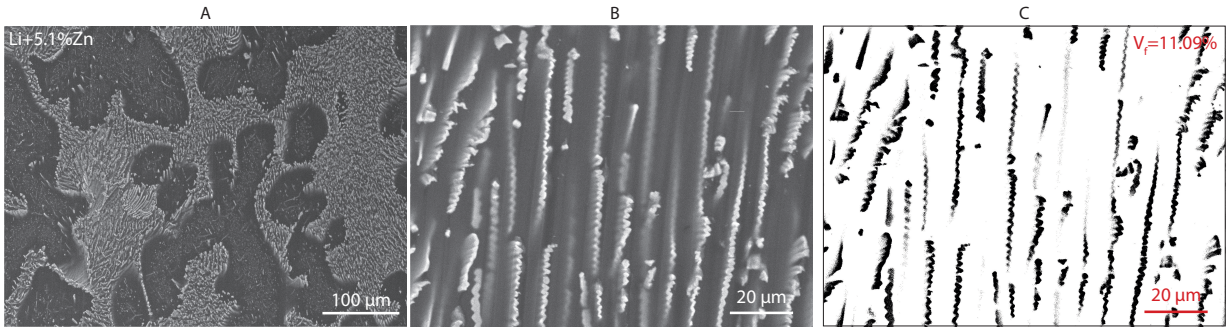

Figure S4: Li+5.1%Zn characterisation. (a) SEM micrograph of air cooled Li+5.1%Zn alloy, showing clear primary Li dendrites surrounded by eutectic matrix. (b) SEM micrograph of furnace cooled Li+5.1%Zn eutectic region. (c) Threshold analysed image from b, identifying volume fraction as 11.09%, giving eutectic composition of Li+7.6%Zn with $V_m^{LiZn} = 18.12\ cm^3\ mol^{-1}$ and $V_m^{Li} = 13.02\ cm^3\ mol^{-1}$

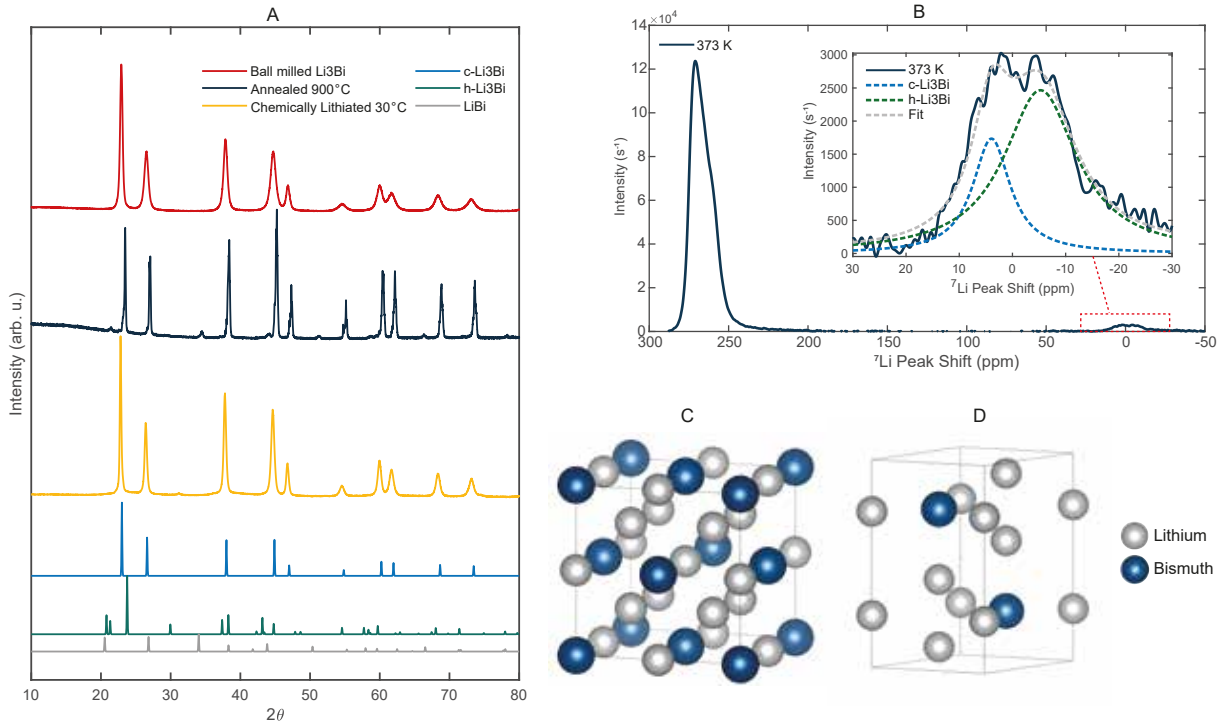

Figure S5: (a) X-ray diffraction of samples produced at the Li_3Bi composition. Ball milled Li_3Bi powder, annealed ball milled powder at 900°C for 3 hours (Some LiBi was observed from lithium loss on annealing) , chemically lithiating bismuth powder with 1M Li-biphenyl solution in tetrahydrofuran (THF) at ambient temperature [11]. All show the c-Li_3Bi structure. (b) Crystal structure of c-Li_3Bi (c)Crystal structure of h-Li_3Bi

Supplementary note 4: Li+1%Mg Performance

Discharge chronopotentiometry at a low current density of 0.3 mA cm^{-2} of a pure lithium metal 100 µm foil self-symmetric cell at 30°C and 2.5 MPa of stack pressure is shown in Figure S6A. By comparison a lithium +

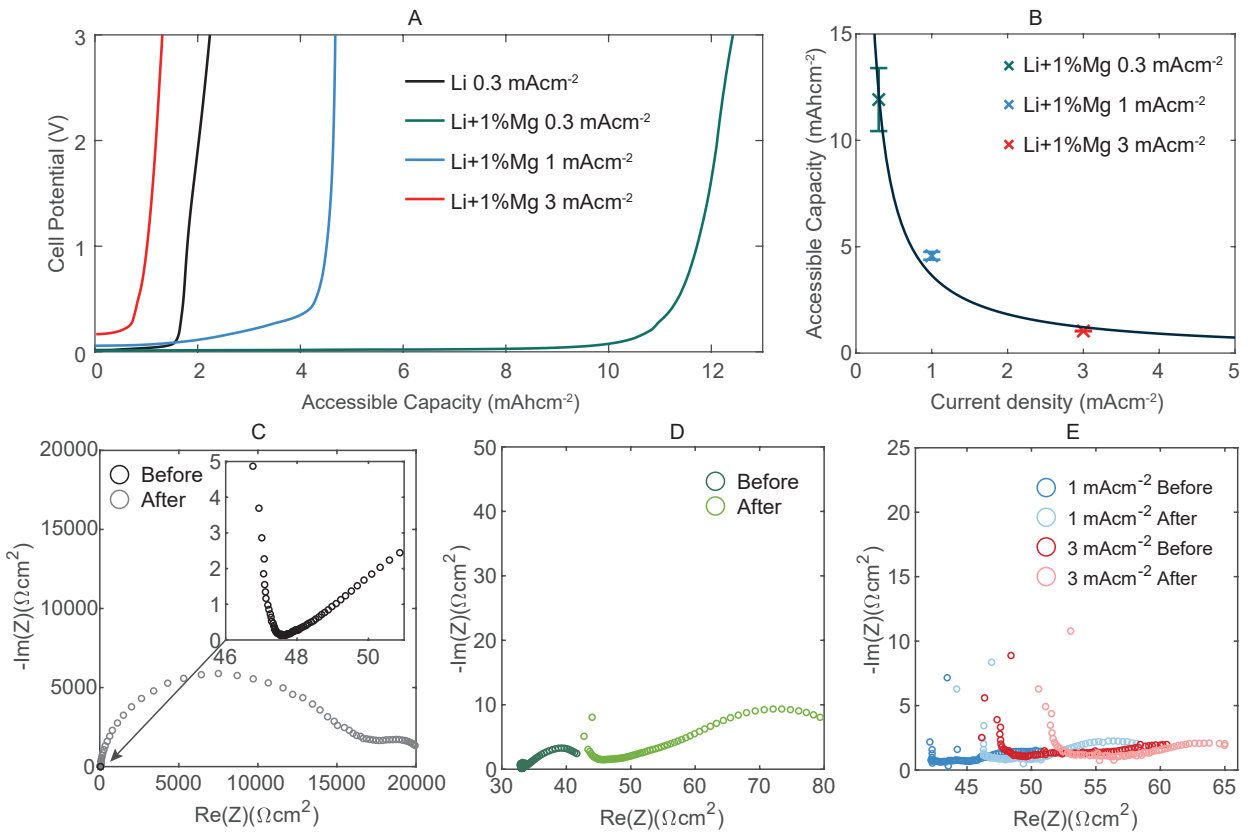

Figure S6: Lithium and Li+1%Mg discharge performance. (a) Chronopotentiometric discharge of Li|Li_6PS_5Cl|Li and Li+1%Mg|Li_6PS_5Cl|Li+1%Mg self symmetric cells at 0.3 $mAcm^{-2}$ and Li+1%Mg|Li_6PS_5Cl|InLi/In cells at 1 and 3 $mAcm^{-2}$, potential shifted up by 0.622 V for easy comparison in cells with InLi/In electrode [4]. (b) Accessible areal capacity against current density for Li+1%Mg cells. (c) EIS spectra before and after discharge at 0.3 $mAcm^{-2}$ for Li|Li_6PS_5Cl|Li self-symmetric cell. (d) EIS spectra before and after discharge at 0.3 $mAcm^{-2}$ for Li+1%Mg|Li_6PS_5Cl|Li+1%Mg self-symmetric cell. (e) EIS spectra before and after discharge at 1 and 3 $mAcm^{-2}$ for Li+1%Mg|Li_6PS_5Cl|InLi/In cells.

1% magnesium solid solution alloy foil discharged in the same conditions delivers significantly higher capacity. The accessible capacity for the Li+1%Mg electrode decreases as current density is increased. This can be seen in Figure S6B showing the accessible capacity up to an equivalent cell potential of 1 V (0.378 V cell potential with InLi/In counter electrode). This accessible capacity at 1 $mA\,cm^{-2}$ is 4.6 ± 0.2 $mAh\,cm^{-2}$ and for 3 $mA\,cm^{-2}$ it is 1.04 ± 0.01 $mAh\,cm^{-2}$. The data confirms the expected inverse relationship between current density and accessible capacity (cap = 3.65/i) for diffusion-limited conditions. This inverse relationship emerges in theoretical derivations of an evolving concentration gradient with a constant interfacial flux at a semi-infinite boundary for a constant diffusivity media.

Electrochemical impedance spectroscopy (EIS) shown in Figure S6C taken for the lithium metal cell before and after discharge, shows an increase in cell potential to very high interfacial impedance over 20 $k\Omega\,cm^2$ indicative of near-total contact loss. By comparison a lithium + 1% magnesium solid solution alloy discharged in the same conditions delivers significantly higher capacity, and EIS taken in the same way shown in Figure S6D shows only a small increase in interfacial impedance. This demonstrates the electrode remains in good contact with the solid electrolyte, even at the very high discharge cell potential of 2.5 V. This effect is discussed in a previous work, where the accessible capacity is determined by diffusion, and in such a condition, the performance is independent of stack pressure [1], compared to pure lithium which is well described as a

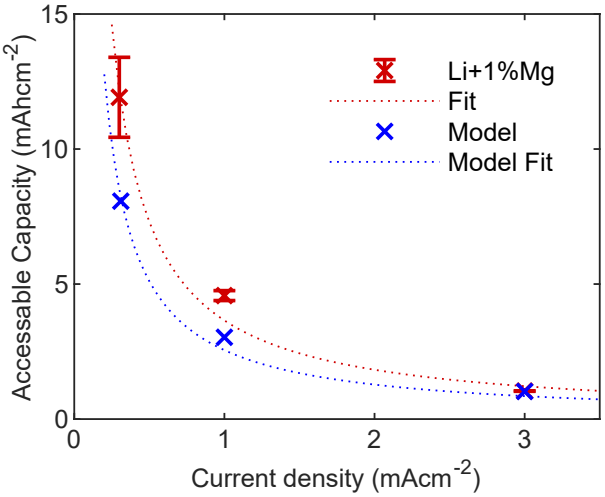

Figure S7: Comparison of experimental and modelled performance for 100 µm Li+1%Mg electrode discharged under a range of current densities at 2.5 MPa, 30 °C.

dynamic balance between plastic deformation and material removal at the interface [13]. Contact loss at the interface leads to current focusing on subsequent cycles [14], accelerating degradation across the whole cell, ultimately driving cell failure. The use of a solid solution alloy as the primary phase therefore has clear benefit in the pursuit of high coulombic efficiency cycling of a solid state battery. Figure S6E shows EIS indicating even better contact retention for Li+1%Mg alloy electrodes at these higher current densities.

References

1. Aspinall, J. *et al.* The impact of magnesium content on lithium-magnesium alloy electrode performance with argyrodite solid electrolyte. *Nature Communications* **15,** 4511. doi:10.1038/s41467-024-48071-0 (2024).
2. Braga, M. H., Dbski, A., Terlicka, S., Gasior, W. & Góral, A. Experimental and ab initio study of the Ag–Li system for energy storage and high-temperature solders. *Journal of Alloys and Compounds* **817.** doi:10.1016/j.jallcom.2019.152811 (2020).
3. Maccio-Figgemeier, V., Eshetu, G. G., Mroz, D., Joo, H. & Figgemeier, E. Establishing Li-acetylide (Li2C2) as functional element in solid-electrolyte interphases in lithium-ion batteries. *Journal of Power Sources Advances* **28,** 100152. doi:10.1016/j.powera.2024.100152 (2024).
4. Aspinall, J. *et al.* Effect of Microstructure on the Cycling Behavior of Li–In Alloy Anodes for Solid-State Batteries. *ACS Energy Letters* **9,** 578–585. doi:10.1021/acsenergylett.3c02274 (2024).
5. Weppner, W. & Huggins, R. A. Electrochemical investigation of the chemical diffusion, partial ionic conductivities, and other kinetic parameters in Li3Sb and Li3Bi. *Journal of Solid State Chemistry* **22,** 297–308. doi:10.1016/0022-4596(77)90006-8 (1977).
6. Ghavidel, M. Z. *et al.* Electrochemical Formation of Four Al-Li Phases (β-AlLi, Al 2 Li 3 , AlLi 2x , Al 4 Li 9) at Intermediate Temperatures. *Journal of The Electrochemical Society* **166,** A4034–A4040. doi:10.1149/2.0061916jes (2019).
7. He, X. *et al.* Tuning Interface Lithiophobicity for Lithium Metal Solid-State Batteries. *ACS Energy Letters* **7,** 131–139. doi:10.1021/acsenergylett.1c02122 (2022).
8. Zheng, T., Zhang, J., Jin, W. & Boles, S. T. Utilization of Li-Rich Phases in Aluminum Anodes for Improved Cycling Performance through Strategic Thermal Control. *ACS Applied Energy Materials* **6,** 1845–1852. doi:10.1021/acsaem.2c03673 (2023).
9. Jia, W. *et al.* A dual-phase Li-Ca alloy with a patternable and lithiophilic 3D framework for improving lithium anode performance. *Journal of Materials Chemistry A* **7,** 22377–22384. doi:10.1039/c9ta08798b (2019).
10. Anani, A., Crouch-Baker, S. & Huggins, R. A. Kinetic and Thermodynamic Parameters of Several Binary Lithium Alloy Negative Electrode Materials at Ambient Temperature. *Journal of The Electrochemical Society* **134,** 3098–3102. doi:10.1149/1.2100347 (1987).
11. Wang, G. *et al.* Chemical Prelithiation of Negative Electrodes in Ambient Air for Advanced Lithium-Ion Batteries. *ACS Applied Materials & Interfaces* **11,** 8699–8703. doi:10.1021/acsami.8b19416 (2019).
12. Beutl, A., Cupid, D. & Flandorfer, H. The Li-Sb phase diagram part I: New experimental results. *Journal of Alloys and Compounds* **695,** 1052–1060. doi:10.1016/j.jallcom.2016.10.230 (2017).
13. Krauskopf, T., Hartmann, H., Zeier, W. G. & Janek, J. Toward a Fundamental Understanding of the Lithium Metal Anode in Solid-State Batteries - An Electrochemo-Mechanical Study on the Garnet-Type Solid Electrolyte Li 6.25 Al 0.25 La 3 Zr 2 O 12. *ACS Applied Materials and Interfaces* **11,** 14463–14477. doi:10.1021/acsami.9b02537 (2019).
14. Kasemchainan, J. *et al.* Critical stripping current leads to dendrite formation on plating in lithium anode solid electrolyte cells. *Nature Materials* **18,** 1105–1111. doi:10.1038/s41563-019-0438-9 (2019).